ATLAS NOTE

ATLAS-CONF-2012-152

November 11, 2012

Search for supersymmetry in final states with jets, missing transverse momentum and a Z boson at $\sqrt{s} = 8$ TeV with the ATLAS detector

The ATLAS Collaboration

Abstract

This note presents a search for supersymmetry in the final state events containing jets, large missing transverse momentum, and a Z boson that decays into electron or muon pairs. The analysis uses a data sample that corresponds to a total integrated luminosity of 5.8 fb^{-1} of $\sqrt{s} = 8$ TeV proton-proton collisions recorded with the ATLAS detector at the Large Hadron Collider. No excess above the Standard Model background expectation is observed. The results are interpreted in the context of a general gauge mediation scenario, where the lightest supersymmetric particle is the gravitino and the next-to-lightest supersymmetric particle is a Higgsino-like neutralino.

ATLAS-CONF-2012-152
12 November 2012

1 Introduction

Supersymmetry (SUSY) [1–9] is one of the most popular extensions of the Standard Model (SM). It provides a solution to the hierarchy problem by postulating the invariance of the theory under a new symmetry which transforms fermions into bosons and vice versa. The minimal supersymmetric extension to the SM (MSSM) [10–14] predicts a supersymmetric partner (or superpartner) for each SM particle that differs in spin by 1/2 from its SM counterpart. In R-parity conserving SUSY [10–14], each supersymmetric interaction involves an even number of supersymmetric particles (sparticles), and as a result the lightest supersymmetric particle (LSP) is stable. In many SUSY models, the LSP serves as a viable candidate for non-baryonic dark matter. Assuming R-parity conservation, SUSY production is characterized by pair-produced sparticles, that then decay via long chains, otherwise known as "cascades", into final states involving LSPs.

Because evidence for supersymmetric particles has not yet been found, if SUSY exists it must be a broken symmetry, allowing the superpartners to be heavier than the corresponding SM particles. One popular scenario that provides a formalism to explain the mechanism of SUSY breaking, which in turn gives rise to the superpartner masses and interactions, is gauge-mediated supersymmetry breaking (GMSB). In GMSB models [15–20], SUSY is broken in a hidden sector and the SUSY breaking is propagated to the visible sector via SM-like $SU(3)_C \times SU(2)_L \times U(1)_Y$ gauge boson and gaugino interactions between some new chiral supermultiplets, called messengers, and the MSSM particles. A distinguishing feature of GMSB models relative to the minimal supergravity [21–25] and anomaly-mediated SUSY breaking models [26, 27] is that scalars with the same gauge quantum numbers, but different flavors, have identical soft SUSY breaking masses. As a result, flavor-changing neutral currents (FCNC) are suppressed.

In GMSB models, the gravitino ($\tilde{G}$) is the LSP. In this note we consider short-lived gravitinos with negligible masses. The gravitino escapes detection, leading to missing transverse momentum (denoted $\mathbf{p}_{\mathrm{T}}^{\mathrm{miss}}$ and its magnitude $E_{\mathrm{T}}^{\mathrm{miss}}$). The phenomenology of GMSB models is determined by the nature of the next-to-lightest supersymmetric particle (NLSP), which for a large part of the GMSB parameter space is the lightest neutralino $\tilde{\chi}_1^0$.

Neutralinos are mixtures of gaugino ($\tilde{B}$, $\tilde{W}^0$) and higgsino ($\tilde{H}_u^0$, $\tilde{H}_d^0$) eigenstates, and therefore the lightest neutralino decays to a $\tilde{G}$ and either a γ, Z, or h. If the $\tilde{\chi}_1^0$ is bino-like, the main decay mode is $\tilde{\chi}_1^0 \to \gamma\tilde{G}$. If the $\tilde{\chi}_1^0$ is higgsino–like, it decays as $\tilde{\chi}_1^0 \to h\tilde{G}$ or $\tilde{\chi}_1^0 \to Z\tilde{G}$. In this scenario, pair production of SUSY particles would lead to two NLSPs resulting in h or Z and $E_{\mathrm{T}}^{\mathrm{miss}}$. By selecting events with at least one Z decaying into an oppositely-charged electron or muon pair and $E_{\mathrm{T}}^{\mathrm{miss}}$, good sensitivity can be obtained over a broad range of SUSY scenarios assuming different $\tilde{\chi}_1^0 \to Z\tilde{G}$ branching ratios.

Searches for GMSB at the Tevatron have been interpreted in minimal GMSB models, where the $\tilde{\chi}_1^0$ is bino–like [28, 29]. In recent years, the effort to formulate GMSB in a more general way has led to the development of general gauge mediation (GGM) [30, 31]. GGM includes an observable sector with all the MSSM fields, together with a hidden sector that contains the source of SUSY breaking.

In GGM, no specific SUSY mass hierarchy is predicted for colored and uncolored states. Unlike in classic GMSB models, the GGM masses for gluinos and squarks, superpartners of gluons and quarks, respectively, can be below the TeV scale and therefore in the reach of the LHC. Both ATLAS and CMS have performed searches for GGM models with a bino–like $\tilde{\chi}_1^0$ [32,33] and wino–like $\tilde{\chi}_1^0$ [34,35]. ATLAS also performed searches for higgsino–like $\tilde{\chi}_1^0$ GGM [36, 37]. No excesses above the SM background expectations were observed.

This analysis presents an updated search for higgsino–like $\tilde{\chi}_1^0$ GGM SUSY models, as suggested in Ref. [38, 39], using a larger dataset and higher center-of-mass energy than the previous searches in Ref. [36]. In these GGM models, the gluino mass, $m(\tilde{g})$, and the higgsino mass parameter, μ, are treated as free parameters. The higgsino mass parameter was chosen to be positive to ensure $\tilde{\chi}_1^0 \to Z\tilde{G}$ is the

dominant NLSP decay. The $U(1)$ and $SU(2)$ gaugino mass parameters (M_1 and M_2) are fixed to 1 TeV. The masses of all other sparticles are fixed at ~1.5 TeV. In this particular region of parameter space, the two lightest neutralinos ($\tilde{\chi}_1^0$ and $\tilde{\chi}_2^0$) and lightest chargino ($\tilde{\chi}_1^\pm$) become higgsino–like. In the limit $(M_1,\ M_2) \to \infty$, the exact relations $m(\tilde{\chi}_1^0) = m(\tilde{\chi}_2^0) = m(\tilde{\chi}_1^\pm) = \mu$ hold true. In practice, M_1 and M_2 are never infinite, and therefore the effect of neutralino and chargino mixing will push the masses of $\tilde{\chi}_1^0, \tilde{\chi}_2^0$ and $\tilde{\chi}_1^\pm$ away from μ. Two different values of tan(β) were used in this analysis. A tan(β) value of 1.5 was chosen, in analogy to the previous 2011 analysis [36], to ensure $\tilde{\chi}_1^0 \to Z\tilde{G}$ is the dominant NLSP decay ($BR(\tilde{\chi}_1^0 \to Z\tilde{G}) \sim 97\%$) [38]. Since large values of tan(β) increase the $BR(\tilde{\chi}_1^0 \to h\tilde{G})$ up to 40%, a tan(β) value of 30 was chosen to investigate models with mixture of $\tilde{\chi}_1^0 \to Z\tilde{G}$ and $\tilde{\chi}_1^0 \to h\tilde{G}$ final states. Finally, the NLSP decay length is fixed to be $c\tau_{\mathrm{NLSP}} < 0.1$ mm.

Gluinos cascade-decay into final states involving the NLSP $\tilde{\chi}_1^0$ and jets via $\tilde{g} \to q\bar{q}\tilde{\chi}_1^0(\tilde{\chi}_2^0)$, followed by the higgsino–like $\tilde{\chi}_1^0$ decay to $Z\tilde{G}$ or $h\tilde{G}$. Depending on the masses of the $\tilde{g}$ and higgsino states, SUSY particle production is dominated either by $\tilde{g}$ pair production (referred to as "strong") or by the production of chargino/neutralino pairs (referred to as "weak"). This analysis focuses on the strong production processes searching for final states that are characterized by the presence of at least one Z boson, which can be detected via its decays to a pair of electrons or muons, large $E_{\mathrm{T}}^{\mathrm{miss}}$, and jets. The $E_{\mathrm{T}}^{\mathrm{miss}}$ results from the undetected gravitinos. The main SM backgrounds are the Z/γ^*+jets, $t\bar{t}$, single-top, and diboson processes. The evaluation of the instrumental Z/γ^* + jets background, which has $E_{\mathrm{T}}^{\mathrm{miss}}$ that is mostly due to hadronic mismeasurement, was made using a data driven method. The WW, $t\bar{t}$, Wt, and $\tau\tau$ backgrounds were estimated from data using $e\mu$ events. The ZZ and WZ backgrounds were estimated using Monte Carlo (MC) simulation. The multijet and inclusive W + jets backgrounds are negligible.

2 ATLAS detector

The ATLAS detector [40] is a general-purpose particle detector with forward-backward symmetric cylindrical geometry[1]. ATLAS consists of inner tracking devices surrounded by a superconducting solenoid, electromagnetic and hadronic calorimeters, and a muon spectrometer inside an air-core toroid magnet system. The inner detector (ID) consists of a silicon pixel detector, a silicon microstrip detector, and a transition radiation tracker. In combination with the 2 T field from the solenoid, the ID provides precision tracking of charged particles for $|\eta| < 2.5$. The calorimeter system covers the pseudorapidity range $|\eta| < 4.9$ and is composed of sampling calorimeters with either liquid argon or scintillating tiles as the active media. The muon spectrometer has separate trigger and high precision tracking chambers which provide muon identification and measurement for $|\eta| < 2.7$.

3 Simulation

Simulated MC event samples were used to model the SUSY signal and to describe the SM background. For the GGM models, the SUSY mass spectra, the gluino branching ratios, and the gluino decay width were calculated using SUSPECT [41] and SDECAY [42]. The MC signal samples were generated using PYTHIA 6.423 [43] with MRST2007 LO* [44] parton distribution functions (PDF).

The signal production rate is dominated at high μ by strong production of gluinos and squarks, but at low μ the direct production of charginos and neutralinos is greatly enhanced. Signal cross sections are calculated to next-to-leading order (NLO) in the strong coupling constant using PROSPINO 2.1 [45] .

[1] ATLAS uses a right-handed coordinate system with its origin at the nominal interaction point in the centre of the detector and the z-axis coinciding with the axis of the beam pipe. The x-axis points from the IP to the center of the LHC ring, and the y-axis points upward. Cylindrical coordinates (r, ϕ) are used in the transverse plane, ϕ being the azimuthal angle around the beam pipe. The pseudorapidity is defined in terms of the polar angle θ as $\eta = -\ln\tan(\theta/2)$. The distance ΔR in the $\eta - \phi$ space is defined as $\Delta R = \sqrt{(\Delta\eta)^2 + (\Delta\phi)^2}$.

The nominal cross section and the uncertainty are taken from an envelope of cross section predictions using different PDF sets and factorization and renormalization scales, as described in Ref. [46]. The PDF sets used for those calculations are CTEQ6.6M and MSTW2008 NLO. The addition of the resummation of soft gluon emission at next to-leading-logarithmic precision (NLL) [47–51] is performed in the case of strong SUSY pair-production.

Single-top and $t\bar{t}$ production were simulated using POWHEG [52] and PYTHIA with the NLO CT10 PDF set. The Z/γ^*+jets, W+jets, and diboson samples were generated using SHERPA [53] with the NLO CT10 PDF set. The Z/γ^* + jets samples were normalized to inclusive next-to-next-to-leading (NNLO) cross-sections [54]. Diboson processes were normalized to NLO cross-sections [55, 56]. A POWHEG sample was used to assess the systematic uncertainties associated with the choice of generator for diboson production.

All samples were processed through the GEANT4 simulation [57, 58] of the ATLAS detector [40]. The in-time and out-of-time pile-up conditions, which result from multiple proton-proton interactions per crossing, were taken into account by overlaying minimum-bias events on the hard-scattering process in each MC sample. The simulated events were then reweighted such that the distribution of the number of interactions per bunch crossing in MC matched the one observed in data.

4 Object and Event Selection

The analysis was performed using data recorded in proton–proton collisions at a center-of-mass energy of 8 TeV, corresponding to an integrated luminosity of $\int \mathcal{L}\,dt = 5.8 \pm 0.2$ fb^{-1} [59] after the application of beam, detector and data quality requirements. Events were selected using dilepton triggers that have constant efficiency as a function of lepton transverse momentum (p_{T}) above the offline p_{T} cuts used in the analysis.

Jets were reconstructed using the anti-k_t jet clustering algorithm [60] with a distance parameter of $R = 0.4$ (in $\eta - \phi$ space). Jets were required to have $p_{\mathrm{T}} > 20$ GeV and to lie within $|\eta| < 4.5$. Electron candidates were required to have $p_{\mathrm{T}} > 10$ GeV and $|\eta| < 2.47$ and pass the "medium" shower shape and track selection criteria [61]. Muon candidates within $|\eta| < 2.4$ were considered, and their p_{T} was required to be greater than 10 GeV. Muons were identified by matching an extrapolated ID track and one or more track segments in the muon spectrometer [62]. The leading lepton in each event was required to have $p_{\mathrm{T}} > 25$ GeV. To avoid double counting, any jet within $\Delta R < 0.2$ of any remaining electron was removed. Finally, electron or muon candidates within $\Delta R < 0.4$ of any remaining jet were also discarded.

The missing transverse momentum was calculated from calorimeter cells with $|\eta| < 4.5$ and from muons. Cells were calibrated according to the object to which they are associated.

After performing the baseline object selection described above, including jet overlap removal, "signal" objects were selected with more stringent requirements. Signal electron candidates were required to pass the "tight" selection criteria [61], which add a requirement on the ratio E/p, where E is the calorimeter cluster energy and p is the track momentum, and the detection of transition radiation. Furthermore, an isolation requirement was imposed by requiring that the sum of the p_{T} of tracks within $\Delta R < 0.2$ around an electron candidate must be less than 10% of the electron p_{T}. Signal muon candidates must have longitudinal and transverse impact parameter values within 1 mm and 0.2 mm of the primary vertex, respectively, and were required to be isolated. The isolation requirement was that the sum of the p_{T} of tracks within $\Delta R < 0.2$ around a muon candidate be less than 1.8 GeV. Signal jets were required to have $p_{\mathrm{T}} > 30$ GeV and $|\eta| < 2.5$. To suppress jet background originating from uncorrelated pileup interactions, more than 50% of the summed p_{T} of all tracks associated to a jet must have come from tracks associated to the selected primary vertex.

Events that contain at least two same-flavor leptons, with the two leading leptons having opposite charge and an invariant mass in a window around the Z boson mass, [81, 101] GeV, were selected. When

Signal Region	SR1	SR2
$E_{\mathrm{T}}^{\mathrm{miss}}$[GeV]	>220	>140
3 leading jets p_{T}[GeV]	>80, >40, >40	-
H_{T}[GeV]	-	>300

Table 1: Criteria for each of the signal regions.

plotting kinematic distributions of the selected events, two representative GGM signal points, which are characterized by the $gg \to \tilde{g}\tilde{g}$ production mechanism, were chosen to illustrate the SUSY contribution:

- $m(\tilde{g}) = 600$ GeV, $\mu = 120$ GeV represents the region $m(\tilde{g}) \gg \mu$.
- $m(\tilde{g}) = 600$ GeV, $\mu = 590$ GeV represents the region $m(\tilde{g}) \approx \mu$.

By examining these GGM grid points, one can see how the SUSY contributions from different kinematic regions behave in the distributions of interest. The source of the $E_{\mathrm{T}}^{\mathrm{miss}}$ in the GGM models is the $\tilde{G}$, which is produced in the decays $\tilde{\chi}_1^0 \to Z\tilde{G}$ and $\tilde{\chi}_1^0 \to h\tilde{G}$. As a result, $E_{\mathrm{T}}^{\mathrm{miss}}$ depends on mass of $\tilde{\chi}_1^0$. This is illustrated in the upper panels of Figure 1, which show the $E_{\mathrm{T}}^{\mathrm{miss}}$ distribution of data and nominal MC simulated events after the Z mass requirement in the ee (left) and $\mu\mu$ (right) channels.

Due to the different kinematics of the GGM signal points, two signal regions (SR) were selected to optimize the GGM search throughout the parameter space [36]. The signal regions, characterized by $E_{\mathrm{T}}^{\mathrm{miss}}$, jet multiplicity, and the scalar sum of the p_{T} of the signal jets and leptons (denoted $H_{\mathrm{T}} \equiv \sum_i p_{\mathrm{T}}^{\mathrm{jet},i} + \sum_i p_{\mathrm{T}}^{\mathrm{lepton},i}$) are defined in Table 1. SR1 was designed to probe events with high jet activity, and the more inclusive SR2 selection allows for better sensitivity in events with fewer jets. The distribution of H_{T} for data and nominal MC events after the Z mass requirement in the ee and $\mu\mu$ channels are shown in the lower panels of Figure 1.

5 Background Evaluation

After applying the SR selection requirements, the dominant SM background processes are Z/γ^* + jets, $t\bar{t}$, Wt, and WW production; these backgrounds were estimated with data-driven techniques. The remaining contributions from WZ and ZZ production were estimated using MC simulation. Multijet and W + jets backgrounds were found to be negligible.

5.1 WW, $t\bar{t}$, Wt, $Z/\gamma^* \to \tau\tau$ background estimation

Since the leptonic decay branching fractions for the ee, $\mu\mu$ and $e\mu$ decays from WW, $t\bar{t}$, Wt, $Z/\gamma^* \to \tau\tau$ are 1:1:2, different-flavor $e\mu$ events were used to estimate the background in the ee and $\mu\mu$ channels from these processes in the SR. The estimation was performed using, for each SR, the relations:

$$N_{ee}^{\mathrm{est}} = \frac{1}{2} N_{e\mu}^{\mathrm{data,corr}} \times k_{ee}, \qquad N_{\mu\mu}^{\mathrm{est}} = \frac{1}{2} N_{e\mu}^{\mathrm{data,corr}} \times k_{\mu\mu}, \tag{1}$$

where $N_{e\mu}^{\mathrm{data,corr}}$ is the number of $e\mu$ events observed in data after applying the SR requirements, corrected for the WZ, ZZ, W + jets, and Z + jets processes in the $e\mu$ channel, which were estimated with MC. The total contribution of these processes is estimated to be negligible in SR1 and < 4% in SR2. k_{ee} and $k_{\mu\mu}$ take into account the differences between the electron and muon reconstruction efficiencies as follows

$$k_{ee} = \sqrt{\frac{N_{ee}^{\mathrm{data}}}{N_{\mu\mu}^{\mathrm{data}}}}, \qquad k_{\mu\mu} = \sqrt{\frac{N_{\mu\mu}^{\mathrm{data}}}{N_{ee}^{\mathrm{data}}}}, \tag{2}$$

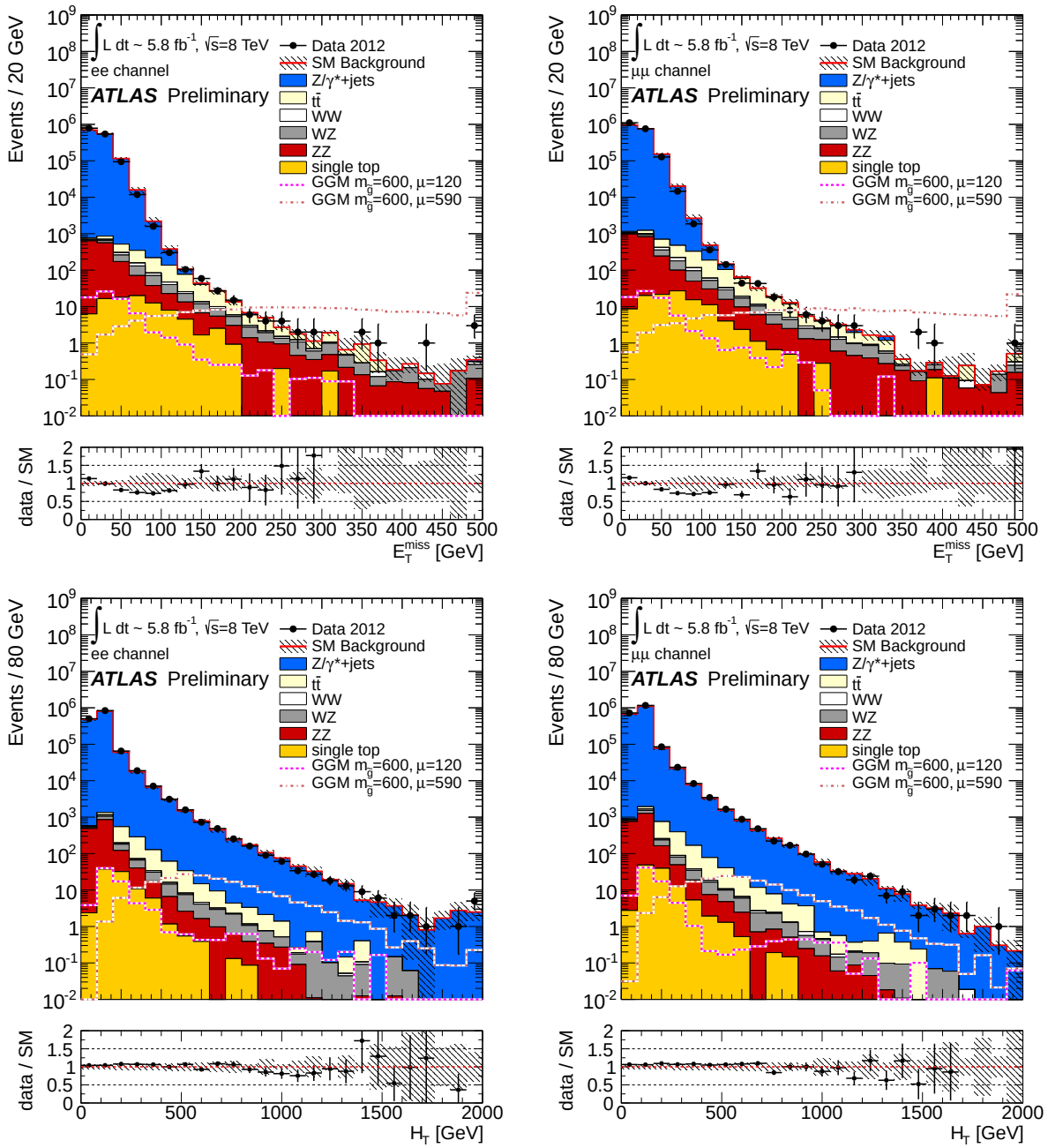

Figure 1: Distribution of $E_{\mathrm{T}}^{\mathrm{miss}}$ (top) and H_{T} (bottom) for data and, for illustration, MC events with nominal cross sections, after $Z \to ee$ (left) and $Z \to \mu\mu$ (right) selections. Two GGM signal points from the $\tan(\beta) = 1.5$ grid are included. The first point was produced with $m(\tilde{g}) = 600$ GeV and $\mu = 120$ GeV, and the second with $m(\tilde{g}) = 600$ GeV and $\mu = 590$ GeV. The plot labeled "data/SM" shows the ratio of the distribution from data to that of the total SM background. The error bars on the data represent statistical uncertainties. The hatched grey band represents the systematic uncertainties on the MC expectations.

Control Region	N_{ee}^{data}	$N_{\mu\mu}^{\text{data}}$	k_{ee}	$k_{\mu\mu}$
CR1	3683	4503	0.91 ± 0.01(stat.)	1.11 ± 0.01(stat.)
CR2	16626	19142	0.93 ± 0.01(stat.)	1.07 ± 0.01(stat.)

Table 2: The number of ee and $\mu\mu$ events and the values of k_{ee} and $k_{\mu\mu}$ estimated from data in the control regions.

where N_{ee}^{data} and $N_{\mu\mu}^{\text{data}}$ are the numbers of ee and $\mu\mu$ events from data in each of the control regions, CR1 and CR2, defined as the corresponding SRs, but with $E_{\text{T}}^{\text{miss}} < 140$ GeV. Signal contamination in the CRs was found to be negligible: less than 0.25% in CR1 and less than 0.15% in CR2. Table 2 summarizes the values of the N_{ee}^{data}, $N_{\mu\mu}^{\text{data}}$, k_{ee}, and $k_{\mu\mu}$ in the control regions.

Systematic uncertainties in the determination of the WW, $t\bar{t}$, Wt, $Z/\gamma^* \to \tau\tau$ backgrounds from the different-flavor samples are due to the subtraction of the MC events from the $e\mu$ data sample, the signal contamination in the signal regions in the $e\mu$ channel and the possible dependence of the lepton reconstruction efficiency on $E_{\text{T}}^{\text{miss}}$. After combining the uncertainties from all sources, the total systematic uncertainty of the estimate for flavor symmetric backgrounds was found to be 9% for SR1 and 5% for SR2.

5.2 Z/γ^* + jets background estimation

After the Z mass requirement, significant SM background stems from Z/γ^* + jets events. Since only $Z/\gamma^* \to ee$ and $Z/\gamma^* \to \mu\mu$ (and not $Z/\gamma^* \to \tau\tau$) decays were selected, this background has $E_{\text{T}}^{\text{miss}}$ that mostly stems from mismeasurement of the reconstructed objects, especially jets. To estimate the contribution of the instrumental Z/γ^* + jets background in the SRs, a "jet smearing" method was used [63]. This method implements a momentum smearing of well-measured jets with a function modeling the response of the calorimeters to determine the acceptance in the SRs for poorly measured Z/γ^* + jets events. The jet response function, estimated for data in Ref. [63], quantifies the probability of fluctuation of the measured p_{T} of jets and takes into account both the effects of jet mis-measurement and contributions from neutrinos and muons in jets from heavy flavor decays. The jet smearing method proceeds in the following steps:

- definition of a seed region, characterized by events with low-$E_{\text{T}}^{\text{miss}}$and well measured jets;
- convolution of jets in the seed events with the response function to generate pseudo-data events;
- validation of the pseudo-data in the control regions;
- validation of the method using an MC-based closure test.

5.2.1 Seed event selection

The selection of the seed events starts from the Z preselected data sample to provide similar topology between seed, control and signal regions. Since there are no jets in a significant fraction of Z preselected events, at least 3 signal jets were required. The seed events were grouped into two regions, one for each SR: ZSeed1 and ZSeed2. Similar kinematics between the seed and the signal regions were ensured by applying the same H_T cut for ZSeed2 as in SR2. To ensure similar hadronic activity in the seed, control

Signal Region	ZSeed1	CR1	ZSeed2	CR2
$E_{\mathrm{T}}^{\mathrm{miss}}$ significance [GeV$^{1/2}$]	< 1.5	-	<1.5	-
$E_{\mathrm{T}}^{\mathrm{miss}}$[GeV]	< 140 GeV			
3 leading jets p_{T}[GeV]	>30, >30, >30	>80, >40, >40	>30, >30, >30	-
f	< 0.4	-	< 0.4	-
H_{T}[GeV]	-	-	>300	>300

Table 3: The cuts defined for the seed and control regions.

and signal regions, the $E_{\mathrm{T}}^{\mathrm{miss}}$significance, which is defined as

$$S = \frac{E_{\mathrm{T}}^{\mathrm{miss}}}{\sqrt{\sum_{i}^{N_{\mathrm{jets}}} p_T^i}}, \tag{3}$$

was used instead of $E_{\mathrm{T}}^{\mathrm{miss}}$ to select events with well measured jets. N_{jets} and p_{T} are the number and the transverse momentum of the reconstructed signal jets in a event. The $E_{\mathrm{T}}^{\mathrm{miss}}$ significance is required to be less than 1.5 GeV$^{1/2}$, which corresonds to $E_{\mathrm{T}}^{\mathrm{miss}}$ less than 50 GeV, for both seed regions.

Since Z/γ^* + jets events at high-$E_{\mathrm{T}}^{\mathrm{miss}}$ tend to have $E_{\mathrm{T}}^{\mathrm{miss}}$ dominated by hadronic mismeasurement, seed events whose $E_{\mathrm{T}}^{\mathrm{miss}}$ is mostly due to contribution from calorimeter cells outside objects should not be selected. This is satisfied by requiring that the fraction, f, of the $E_{\mathrm{T}}^{\mathrm{miss}}$ associated to these cells be less than 0.4. Table 3 summarizes the definitions of seed and control regions used in this method. The signal contamination in the seed region is negligible, < 1%, due to the real source of $E_{\mathrm{T}}^{\mathrm{miss}}$ in these events. The contributions of the non-Z sources in the seed region was also found to be negligible (< 1%).

5.2.2 Jet smearing and generation of the pseudo-data

To smear the momenta of jets in the seed events, the response functions, composed of a Gaussian core and non-Gaussian tails and defined in Ref. [63], were used. As the seed selection is defined such that the jets are mostly well-measured, smearing the jets with these response functions will generate higher-$E_{\mathrm{T}}^{\mathrm{miss}}$ events, known as "pseudo-data", which should provide a shape for the $E_{\mathrm{T}}^{\mathrm{miss}}$ that accurately represents effects from jet mismeasurement. The smeared $E_{\mathrm{T}}^{\mathrm{miss}}$ is derived as:

$$\mathbf{E}_{\mathrm{T}}^{\mathrm{miss}\prime} = \mathbf{E}_{\mathrm{T}}^{\mathrm{miss}} - \sum_i \mathbf{p}_{\mathrm{T}}{}'(j_i) + \sum_i \mathbf{p}_{\mathrm{T}}(j_i) \tag{4}$$

where $\mathbf{E}_{\mathrm{T}}^{\mathrm{miss}}$ ($\mathbf{E}_{\mathrm{T}}^{\mathrm{miss}\prime}$) and $\mathbf{p}_{\mathrm{T}}$ and ($\mathbf{p}_{\mathrm{T}}{}'$) are the unsmeared (smeared) $E_{\mathrm{T}}^{\mathrm{miss}}$ and jet momenta, respectively.

The systematic uncertainties associated with the jet smearing method are due to the fluctuations in the non-Gaussian tails of the response function [63]. This region of the response function is responsible for large jet mis-measurement and is thus the dominant factor in smearing to large $E_{\mathrm{T}}^{\mathrm{miss}}$ values.

5.2.3 Validation of the pseudo-data and MC closure test

Figure 2 shows the $E_{\mathrm{T}}^{\mathrm{miss}}$ of the data and different SM contributions in the control regions in the ee and $\mu\mu$ channels. The Z/γ^* + jets contribution shows the estimate using pseudo-data; top, WW, and $Z/\gamma^* \to \tau\tau$ contributions were estimated with the data-driven method described in Section 5.1. The WZ and ZZ contributions were taken from MC. The pseudo-data are normalized to the data in the region $E_{\mathrm{T}}^{\mathrm{miss}} < 40$ GeV. An MC-based closure test was performed by comparing the $E_{\mathrm{T}}^{\mathrm{miss}}$distribution of fully

	SR1	
	ee	$\mu\mu$
WW, $t\bar{t}$, Wt, $\tau\tau$	1.8 ± 1.1(stat.) ± 0.2(syst.)	2.2 ± 1.3(stat.) ± 0.2(syst.)
WZ	0.7 ± 0.1(stat.) ± 0.3(syst.)	0.5 ± 0.1(stat.) ± 0.2(syst.)
ZZ	0.2 ± 0.03(stat.) ± 0.1(syst.)	0.2 ± 0.03(stat.) ± 0.1(syst.)
Z/γ^* + jets	0.5 ± 0.1(stat.) ± 0.3(syst.)	0.3 ± 0.04(stat.) ± 0.2(syst.)
Total SM Background	3.1 ± 1.1(stat.) ± 0.5(syst.)	3.2 ± 1.3(stat.) ± 0.4(syst.)
Observed	5	5
GGM $(m(\tilde{g}), \mu)$ = (600, 120) GeV	0.3 ± 0.2(stat.) ± 0.01(syst.)	0.1 ± 0.04(stat.) ± 0.1(syst.)
GGM $(m(\tilde{g}), \mu)$ = (600, 590) GeV	52.9 ± 0.9(stat.) ± 11.0(syst.)	47.3 ± 0.9(stat.) ± 9.8(syst.)
$\sigma^{95\%}_{\mathrm{BSM,max}} \cdot A \cdot \epsilon$ (exp) [fb]	1.3	
$\sigma^{95\%}_{\mathrm{BSM,max}} \cdot A \cdot \epsilon$ (obs) [fb]	2.0	

Table 4: Expected SM background event yields and number of events observed in data for an integrated luminosity of 5.8 fb^{-1} after the SR1 requirements for the electron and muon channels. In addition, yields are given for the two representative tan(β) = 1.5 GGM grid points (presented in Figures 1, 2, and 3). Finally, the observed and expected 95% CL upper limits on the visible cross section for SR1 selection are shown.

simulated Z/γ^* + jets samples with that of events obtained with a jet smearing method using an MC-based response function. Satisfactory agreement between these samples was found, and no additional systematic uncertainty was added.

6 Systematic Uncertainties

Systematic uncertainties affecting the background rate and SUSY signal yields in the signal regions have been evaluated.

The systematic uncertainties for the data-driven evaluation of WW, $t\bar{t}$, Wt, $Z/\gamma^* \to \tau\tau$ background were found to be 9% for SR1 and 5% for SR2. The systematic uncertainties on the data-driven estimates of the Z/γ^* + jets background were found to be 70% (80%) for SR1 and 50% (67%) for SR2 for the electron (muon) channel. The total uncertainty on the MC WZ prediction was estimated to be 46% (46%) for SR1 and 21% (23%) for SR2 for the electron (muon) channel. The uncertainty on the MC ZZ estimate was found to be 28% (38%) for SR1 and 10% (19%) for SR2 for the electron (muon) channel. The uncertainties for these MC estimated backgrounds are dominated by the uncertainty on the jet energy scale and the uncertainty due to the choice of generators.

For the GGM signal processes, the total cross-section uncertainties vary from 3 to 34% depending of the SUSY particle production in the signal models. The systematic uncertainties due to experimental sources were also assessed for signal MC.

7 Results

Tables 4 and 5 show the number of expected events in the SRs for each background source together with the observed number of events. Good agreement is observed between data and SM expectations within uncertainties. These tables also show the 95% confidence-level upper bound $\sigma^{95\%}_{\mathrm{BSM,max}} \cdot A \cdot \epsilon$ on the cross section times efficiency within acceptance for the corresponding selection as well as yields for the two reference GGM grid points. In Figure 3 the distributions of $E_{\mathrm{T}}^{\mathrm{miss}}$ for data and SM expectations in the ee and $\mu\mu$ channels after application of the SR1 and SR2 requirements, except for the $E_{\mathrm{T}}^{\mathrm{miss}}$ cut, are shown.

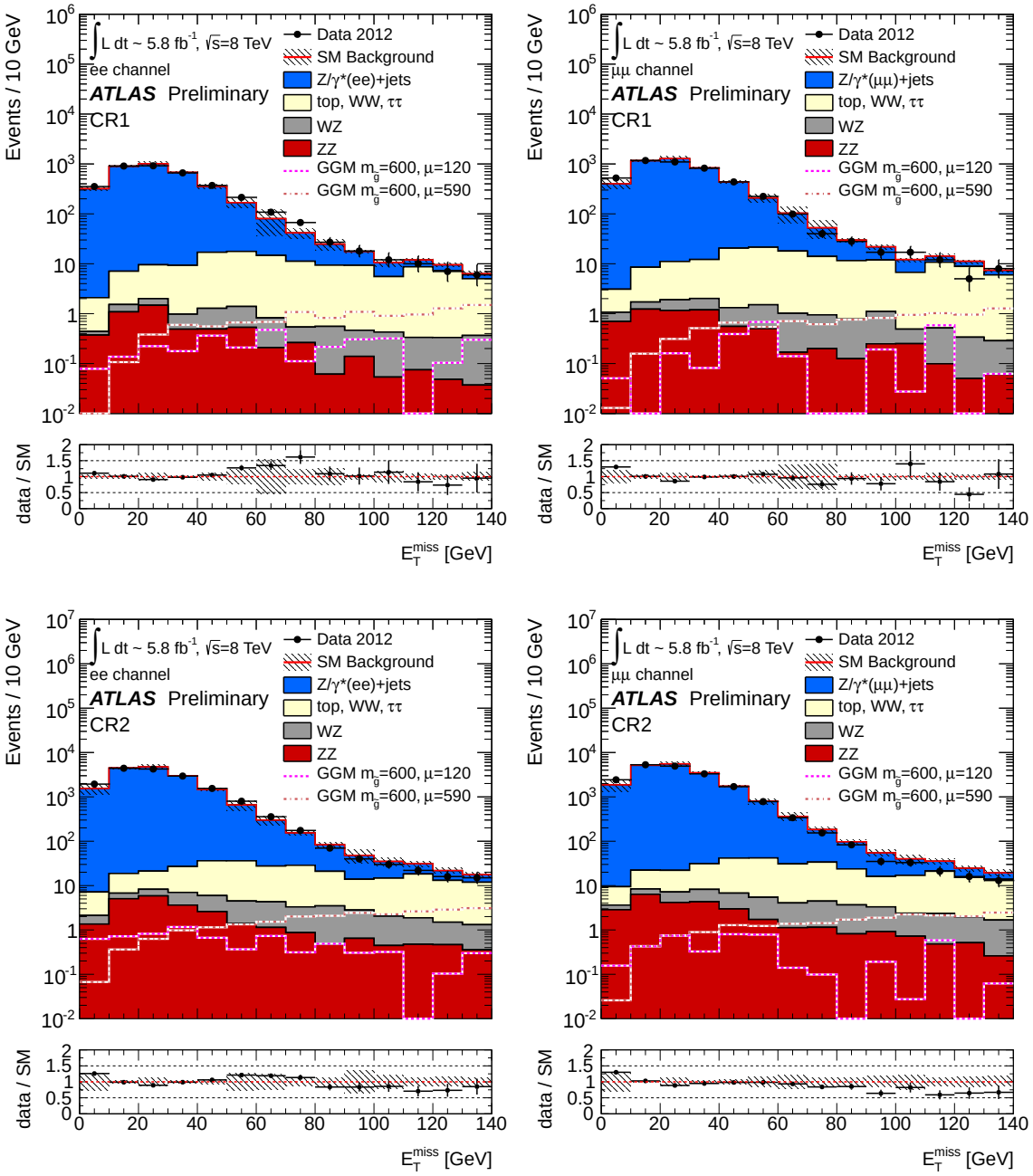

Figure 2: $E_{\mathrm{T}}^{\mathrm{miss}}$ distributions in CR1 (top) and CR2 (bottom), in the ee (left) and $\mu\mu$ (right) channels. The black points represent selected data. The Z/γ^*+jets contribution comes from the data-driven jet smearing method, the top+WW+$\tau\tau$ contribution comes from the data-driven $e\mu$ sample method, and the WZ and ZZ contributions come directly from MC. The hatched grey band represents the systematic uncertainties on the Z/γ^* + jets estimation and the MC expectations for WZ and ZZ.

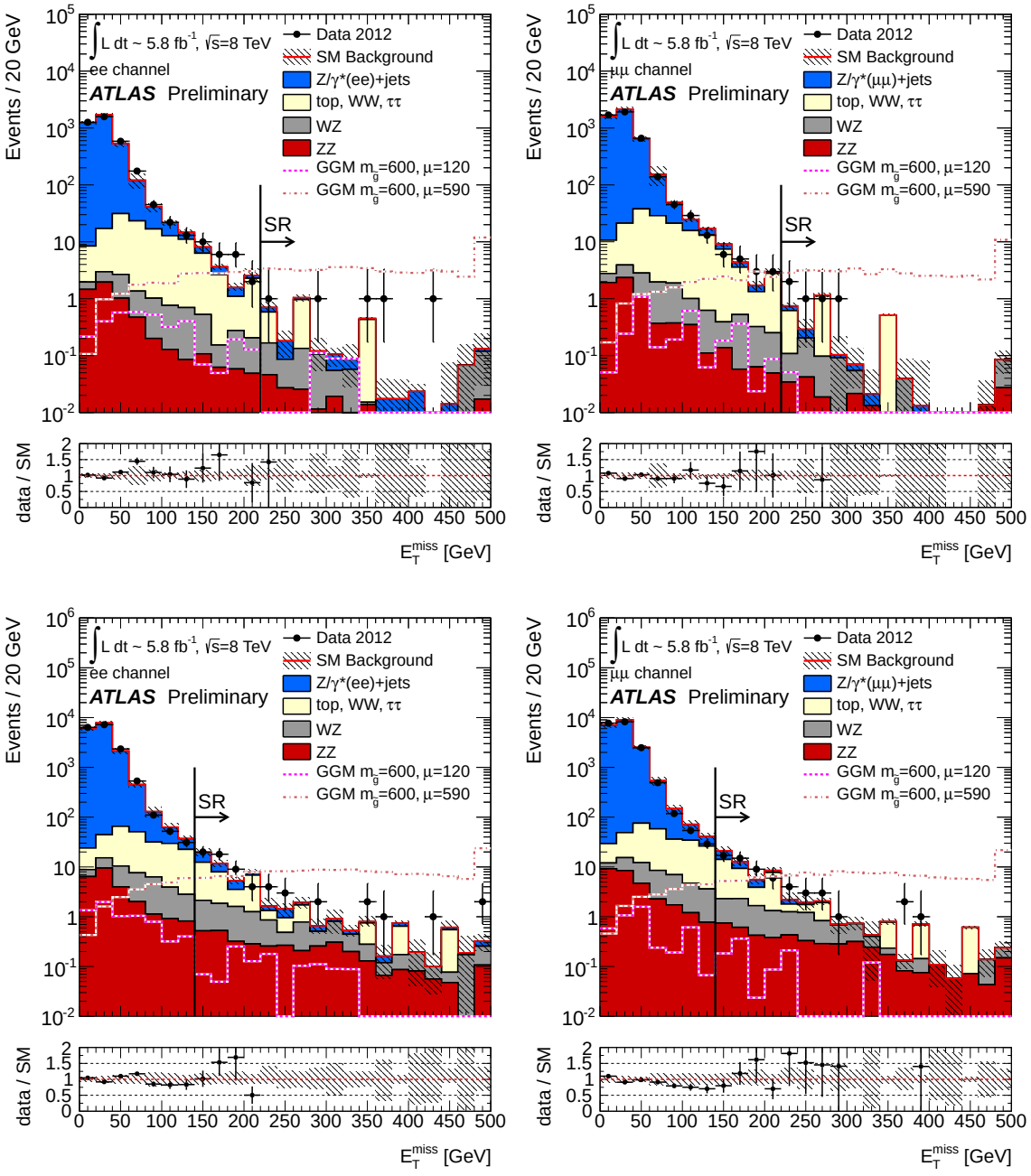

Figure 3: $E_{\mathrm{T}}^{\mathrm{miss}}$ distributions in SR1 (top) and SR2 (bottom), before any cuts on $E_{\mathrm{T}}^{\mathrm{miss}}$, in the *ee* (left) and $\mu\mu$ (right) channels. The black points represent selected data. The Z/γ^* + jets contribution comes from the data-driven jet smearing method, the top+WW+$\tau\tau$ contribution is from the data-driven $e\mu$ sample method, and the WZ and ZZ contributions come directly from MC. The hatched grey band represents the systematic uncertainties on the Z/γ^* + jets estimation and the MC expectations for WZ and ZZ.

	SR2	
	ee	$\mu\mu$
WW, $t\bar{t}$, Wt, $\tau\tau$	26.9 ± 3.8(stat.) ± 1.7(syst.)	30.9 ± 4.3(stat.) ± 1.8(syst.)
WZ	8.4 ± 0.5(stat.) ± 1.8(syst.)	9.0 ± 0.5(stat.) ± 2.1(syst.)
ZZ	3.7 ± 0.1(stat.) ± 0.4(syst.)	4.8 ± 0.2(stat.) ± 0.9(syst.)
Z/γ^* + jets	17.0 ± 0.6(stat.) ± 8.1(syst.)	14.8 ± 0.5(stat.) ± 10.0(syst.)
Total SM Background	55.9± 3.9(stat.) ± 8.4(syst.)	59.5± 4.4(stat.) ± 10.4(syst.)
Observed	66	61
GGM $(m(\tilde{g}), \mu)$ = (600, 120) GeV	1.1 ± 0.3(stat.) ± 0.2(syst.)	1.0 ± 0.3(stat.) ± 0.2(syst.)
GGM $(m(\tilde{g}), \mu)$ = (600, 590) GeV	151.8 ± 1.6(stat.) ± 28.9(syst.)	133.8 ± 1.5(stat.) ± 25.8(syst.)
$\sigma^{95\%}_{\mathrm{BSM,max}} \cdot A \cdot \epsilon$ (exp) [fb]	6.3	
$\sigma^{95\%}_{\mathrm{BSM,max}} \cdot A \cdot \epsilon$ (obs) [fb]	7.7	

Table 5: Expected SM background event yields and number of events observed in data for an integrated luminosity of 5.8 fb^{-1} after the SR2 requirements for the electron and muon channels. In addition, yields are given for the two representative tan(β) = 1.5 GGM grid points (presented in Figures 1, 2, and 3). Finally, the observed and expected 95% CL upper limits on the visible cross section for SR2 selection are shown.

8 Interpretation

In the SRs, the expectation from SM and observation agree within uncertainties. As the number of observed events in consistent with the SM prediction, the results of the analysis are interpreted as 95% confidence level (CL) exclusion limits on $m(\tilde{g})$ and μ in the higgsino-like NLSP scenario defined for the GGM model grids. The expected and observed 95% CL upper limits were computed using the CL_s method [64] combining the ee and $\mu\mu$ channels. Systematic uncertainties were treated as nuisance parameters, and their correlations were taken into account.

The observations in the SRs were first interpreted in the context of the low tan(β) GGM grid, which is characterized by a high $BR(\tilde{\chi}^0_1 \rightarrow Z\tilde{G})$. Figure 4 shows the exclusion limit for this interpretation using results from SR1. Because the upper expected limits computed at each point in the GGM grid are stronger in the case of SR1, SR2 results do not enter the computation. For the range $180 < \mu < 800$ GeV, an upper limit of 680 – 880 GeV is placed on the gluino mass. In addition to the results presented in this analysis, the excluded region from the 2011 $Z + E_{\mathrm{T}}^{\mathrm{miss}}$ analysis [36] is shown.

Te results of the analysis were also interpreted using models with tan(β) = 30. This is the first interpretation using such models in ATLAS. Figure 5 shows the exclusion limit for SR1 using this high-tan(β) interpretation. Again, the expected upper limits are stronger across the grid for SR1, and therefore SR2 results do not contribute. For the range $180 < \mu < 740$ GeV, an upper limit of 680 – 820 GeV is placed on the gluino mass.

9 Conclusions

A search for events with large $E_{\mathrm{T}}^{\mathrm{miss}}$ and a Z boson that decays to a pair of electrons or muons has been performed using 5.8 fb^{-1} of ATLAS data collected in 2012. With no excess observed in the selected signal regions, limits on $m(\tilde{g})$ and μ have been derived in the context of GGM, when the lightest neutralino NLSP is higgsino-like. Assuming tan(β) = 1.5, $M_1 = M_2 = 1$ TeV, and $c\tau_{\mathrm{NLSP}} < 0.1$ mm, gluino masses up to 680 – 880 GeV are excluded at 95% CL for masses of $\tilde{\chi}^0_1$ in the range 160 – 760 GeV. To probe the GGM parameter space at larger values of tan(β), an interpretation with tan(β) = 30 was also performed. Using these signal models, gluino masses of 680 – 820 GeV are excluded at 95% CL for masses of $\tilde{\chi}^0_1$ in the range 160 – 720 GeV.

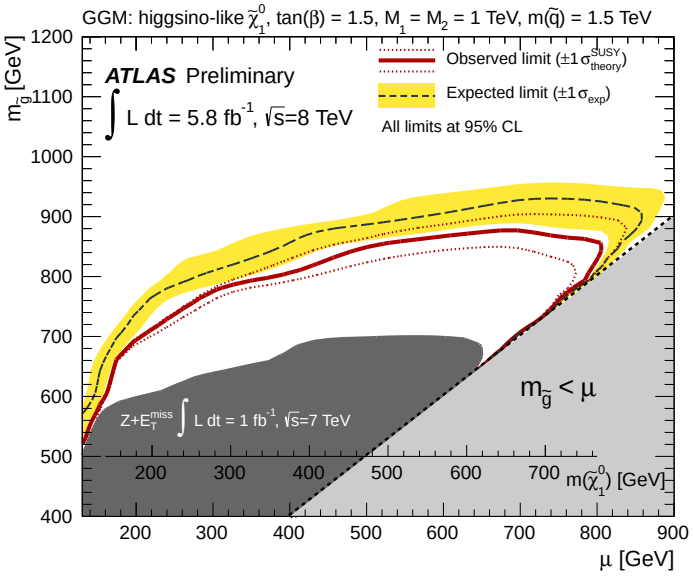

Figure 4: Expected and observed 95% CL exclusion limits for SR1 on the $m(\tilde{g})$ and μ parameters for GGM models with $\tan(\beta) = 1.5$, $M_1 = M_2 = 1$ TeV, $c\tau_{\text{NLSP}} < 0.1$ mm, and $m(\tilde{q}) = 1.5$ TeV. An additional axis corresponding to $m(\tilde{\chi}_1^0)$ is provided. The dark grey area shows the observed exclusion based on the analysis in Ref. [36]. The light grey area indicates the region where the NLSP is the gluino, which is not considered in this analysis.

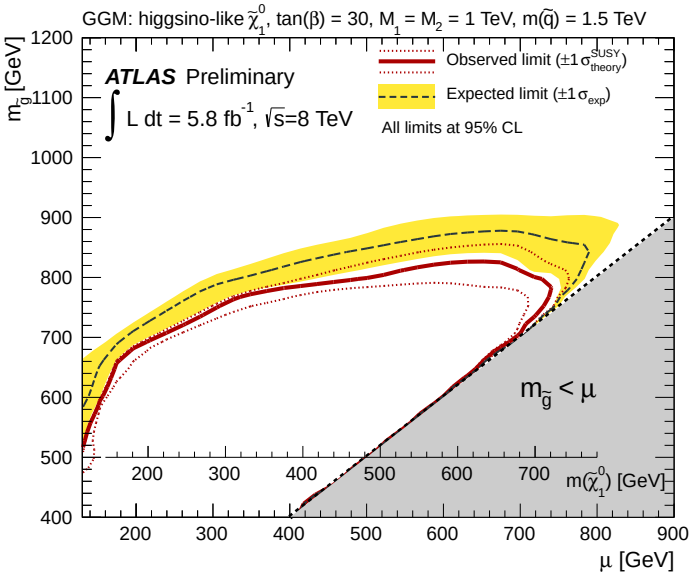

Figure 5: Expected and observed 95% CL exclusion limits for SR1 on the $m(\tilde{g})$ and μ parameters for GGM models with $\tan(\beta) = 30$, $M_1 = M_2 = 1$ TeV, $c\tau_{\text{NLSP}} < 0.1$ mm, and $m(\tilde{q}) = 1.5$ TeV. An additional axis corresponding to $m(\tilde{\chi}_1^0)$ is provided. The light grey area indicates the region where the NLSP is the gluino, which is not considered in this analysis.

References

[1] H. Miyazawa, Prog. Theor. Phys. **36 (6)** (1966) 1266–1276.

[2] P. Ramond, Phys. Rev. **D3** (1971) 2415–2418.

[3] Y. A. Golfand and E. P. Likhtman, JETP Lett. **13** (1971) 323–326.

[4] A. Neveu and J. H. Schwarz, Nucl. Phys. **B31** (1971) 86–112.

[5] A. Neveu and J. H. Schwarz, Phys. Rev. **D4** (1971) 1109–1111.

[6] J. Gervais and B. Sakita, Nucl. Phys. **B34** (1971) 632–639.

[7] D. V. Volkov and V. P. Akulov, Phys. Lett. **B46** (1973) 109–110.

[8] J. Wess and B. Zumino, Phys. Lett. **B49** (1974) 52.

[9] J. Wess and B. Zumino, Nucl. Phys. **B70** (1974) 39–50.

[10] P. Fayet, Phys. Lett. **B64** (1976) 159.

[11] P. Fayet, Phys. Lett. **B69** (1977) 489.

[12] G. R. Farrar and P. Fayet, Phys. Lett. **B76** (1978) 575–579.

[13] P. Fayet, Phys. Lett. **B84** (1979) 416.

[14] S. Dimopoulos and H. Georgi, Nucl. Phys. **B193** (1981) 150.

[15] M. Dine and W. Fischler, Phys. Lett. **B110** (1982) 227.

[16] L. Alvarez-Gaume et al., Nucl. Phys. **B207** (1982) 96.

[17] C. R. Nappi and B. A. Ovrut, Phys. Lett. **B113** (1982) 175.

[18] M. Dine and A. E. Nelson, Phys. Rev. **D48** (1993) 1277–1287, [arXiv:hep-ph/9303230].

[19] M. Dine et al., Phys. Rev. **D51** (1995) 1362–1370, [arXiv:hep-ph/9408384].

[20] M. Dine et al., Phys. Rev. **D53** (1996) 2658–2669, [arXiv:hep-ph/9507378].

[21] A. H. Chamseddine, R. L. Arnowitt, and P. Nath, Phys.Rev.Lett. **49** (1982) 970.

[22] R. Barbieri, S. Ferrara, and C. A. Savoy, Phys.Lett. **B119** (1982) 343.

[23] L. E. Ibanez, Phys.Lett. **B118** (1982) 73.

[24] L. J. Hall, J. D. Lykken, and S. Weinberg, Phys.Rev. **D27** (1983) 2359–2378.

[25] N. Ohta, Prog.Theor.Phys. **70** (1983) 542.

[26] G. F. Giudice, M. A. Luty, et al., JHEP **9812** (1998) 027, [arXiv:hep-ph/9810442].

[27] L. Randall and R. Sundrum, Nucl.Phys. **B557** (1999) 79–118, [arXiv:hep-th/9810155].

[28] CDF Collaboration, Phys. Rev. Lett. **104** (2010) 011801, [arXiv:0910.3606].

[29] D0 Collaboration, Phys. Rev. Lett. **105** (2010) 221802, [arXiv:1008.2133].

[30] P. Meade et al., Prog. Theor. Phys. Suppl. **177** (2009) 143–158, [arXiv:0801.3278].

[31] M. Buican et al., JHEP **03** (2009) 016, [arXiv:0812.3668].

[32] ATLAS Collaboration, Phys. Lett. **B710** (2012) 519–537, [arXiv:1111.4116].

[33] CMS Collaboration, Phys. Rev. Lett. **106** (2011) 211802, [arXiv:1103.0953].

[34] CMS Collaboration, JHEP **1106** (2011) 093, [arXiv:1105.3152].

[35] ATLAS Collaboration, ATLAS-CONF-2012-144 , http://cdsweb.cern.ch/record/1485660 (2012).

[36] ATLAS Collaboration, ATLAS-CONF-2012-046, http://cdsweb.cern.ch/record/1448222 (2012).

[37] ATLAS Collaboration, [arXiv:1211.1167].

[38] P. Meade, M. Reece, et al., JHEP **1005** (2010) 105, [arXiv:0911.4130].

[39] J. T. Ruderman and D. Shih, JHEP **1208** (2012) 159, [arXiv:1103.6083].

[40] ATLAS Collaboration, JINST **3** (2008) S08003.

[41] A. Djouadi et al., Comput. Phys. Commun. **176** (2007) 426–455, [arXiv:hep-ph/0211331].

[42] M. Muhlleitner et al., Comput. Phys. Commun. **168** (2005) 46–70, [arXiv:hep-ph/0311167].

[43] T. Sjostrand et al., JHEP **05** (2006) 026, [arXiv:hep-ph/0603175].

[44] A. Sherstnev and R. Thorne, Eur. Phys. J. **C55** (2008) 553–575, [arXiv:0711.2473].

[45] W. Beenakker et al., [arXiv:hep-ph/9611232].

[46] M. Kramer et al., CERN-PH-TH-2012-163, http://cdsweb.cern.ch/record/1456029 (2011).

[47] W. Beenakker and R. Hopker, Nucl. Phys. **B492** (1997) 51–103, [arXiv:hep-ph/9610490].

[48] A. Kulesza and L. Motyka, Phys. Rev. Lett. **102** (2009) 111802, [arXiv:0807.2405].

[49] A. Kulesza and L. Motyka, Phys. Rev. **D80** (2009) 095004, [arXiv:0905.4749].

[50] W. Beenakker and S. Brensing, JHEP **0912** (2009) 041, [arXiv:0909.4418].

[51] W. Beenakker and S. Brensing, Int. J. Mod. Phys. **A26** (2011) 2637–2664, [arXiv:1105.1110].

[52] S. Frixione et al., JHEP **11** (2007) 070, [arXiv:0709.2092].

[53] T. Gleisberg, S. Hoeche, et al., JHEP **0902** (2009) 007, [arXiv:0811.4622].

[54] K. Melnikov and F. Petriello, Phys. Rev. **D74** (2006) 114017, [arXiv:hep-ph/0609070].

[55] J. M. Campbell, R. K. Ellis, et al., JHEP **1107** (2011) 018, [arXiv:1105.0020].

[56] J. M. Campbell and R. K. Ellis, Phys. Rev. **D60** (1999) 113006, [arXiv:hep-ph/9905386].

[57] GEANT4 Collaboration, Nucl. Instrum. Meth. **A506** (2003) 250–303.

[58] ATLAS Collaboration, Eur. Phys. J. **C70** (2010) 823–874, [arXiv:1005.4568].

[59] ATLAS Collaboration, Eur. Phys. J. **C71** (2011) 1630, [arXiv:1101.2185].

[60] M. Cacciari et al., JHEP **0804** (2008) 063, [arXiv:hep-ph/0802.1189].

[61] ATLAS Collaboration, Eur. Phys. J. **C72** (2012) 1909, [arXiv:1110.3174].

[62] ATLAS Collaboration, ATLAS-CONF-2011-063, http://cdsweb.cern.ch/record/1345743 (2011).

[63] ATLAS Collaboration, CERN-PH-EP-2012-195, http://cdsweb.cern.ch/record/1472021 (2012).

[64] A. L. Read, J. Phys. **G28** (2002) 2693–2704.